

Electronic Supplementary Information (ESI)

Fabrication of an Advanced Asymmetric Supercapacitor based on Microcubical PB@MnO₂ Hybrid and PANI/GNP Composite with Excellent Electrochemical Behaviour

Amit Kumar Das, Ranadip Bera, Anirban Maitra, Sumanta Kumar Karan, Sarbaranjan Paria, Lopamudra Halder, Suman Kumar Si, Aswini Bera, Bhanu Bhusan Khatua*

Materials Science Centre, Indian Institute of Technology Kharagpur, Kharagpur-721302,

West Bengal, India

***Corresponding Author**

Dr. B.B. Khatua (*Email:* khatuabb@matsc.iitkgp.ernet.in).

Materials Science Centre, Indian Institute of Technology, Kharagpur –721302, India.

Tel.:91-3222-283982

Experimental

Preparation of the Electrode Material

Synthesis of PANI/GNP (PG) composite

For the preparation of the PG composite, a very simple and facile process of oxidative in-situ polymerization of aniline in presence of dispersed GNP was followed, as reported in our previous research work.¹ Briefly, 100 mL of 1 M HCl solution was sonicated for 25 min with 40 mg GNP and 0.5 g CTAB which helps to facilitate the uniform dispersion of GNP in the acidic solution. Then, this dispersed suspension was vigorously stirred for another 10 min on a magnetic stirrer. Finally, 1 mL aniline was added to the dispersion followed by gentle addition of APS solution (1 gm APS in 100 ml 1 M HCl) and the mixture turned bluish green after around 3 min. This polymerization reaction was still continued for further 5 h at room temperature and then filtered. The residue was washed with DI water and ethanol several times and dried overnight at 60 °C in an air-oven. For comparison, pure PANI was also prepared in a similar method.

Results and discussion

Structural Characterizations

FTIR Analysis

Fig. S1 represents the typical FTIR spectra of pure PANI and PG composite in the range of 4000 – 450 cm^{-1} with 4 cm^{-1} resolution. The bands at 1562 cm^{-1} and 1483 cm^{-1} in the FTIR spectrum of PANI (Fig. S1a) indicate the stretching vibration of C=C bond in quinoid and benzenoid rings, respectively.² The low intense peaks within the range of 3500–3000 cm^{-1} and 3000–2800 cm^{-1} belong to the N–H and C–H bond stretching, respectively. Two additional characteristic peaks at around 1288 cm^{-1} and 1236 cm^{-1} are ascribable to the C–N stretching mode in quinoid-benzenoid-quinoid unit and benzenoid ring, respectively and some other peaks roughly at 1103 cm^{-1} , 866 cm^{-1} and 790 cm^{-1} are indicative of the in-plane

C–H bending in quinoid and benzenoid units and out-of-plane C–H bending in the aromatic ring, respectively.³ The graphitic double bonds present in the PG composite was confirmed from the peak at around 1626 cm^{-1} as detected in its FTIR spectrum (Fig. S1b).⁴ Presence of different bands of PANI in the FTIR spectrum of PG composite with a little shift in position has been shown by dotted lines (Fig. S1). The shifting in the bands are the consequences of mutual interactions which led to the structural change in the polymer backbone.

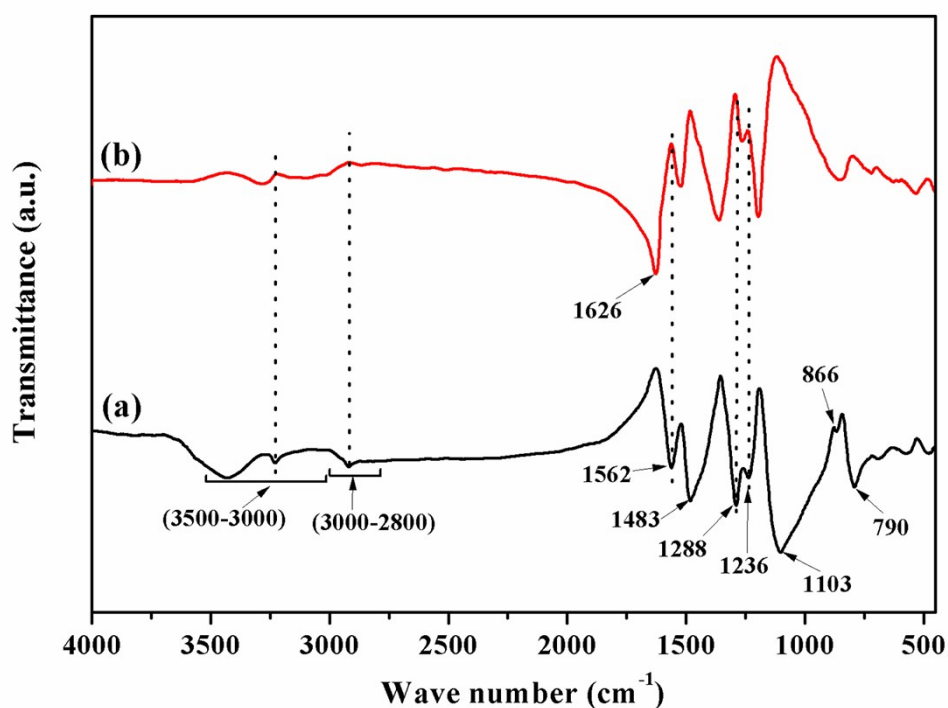


Fig. S1 FTIR spectra of (a) pure PANI and (b) PG composite.

Wide Angle X-Ray Diffraction (WAXD) Study

To explore the crystal structures of the as-synthesized pure PANI and PG composite, WAXD analysis was done and the obtained XRD patterns are shown in Fig. S2. The sharp peaks at $2\theta = 14.8^\circ$, 20.6° and 25.4° in the X-ray diffractogram of pure PANI (Fig. S2a) denote the (011), (020) and (200) crystal planes of PANI in emeraldine salt form, respectively.⁵ Along with all the afore-mentioned peaks for PANI (shown by dotted lines in the figure), the additional peaks obtained at $2\theta = 26.4^\circ$, 42.7° , 44.1° and 54.6° for the XRD

pattern of the PG composite (Fig. S2b) are ascribable to the (002), (100), (101) and (004) crystal planes of GNP.⁶

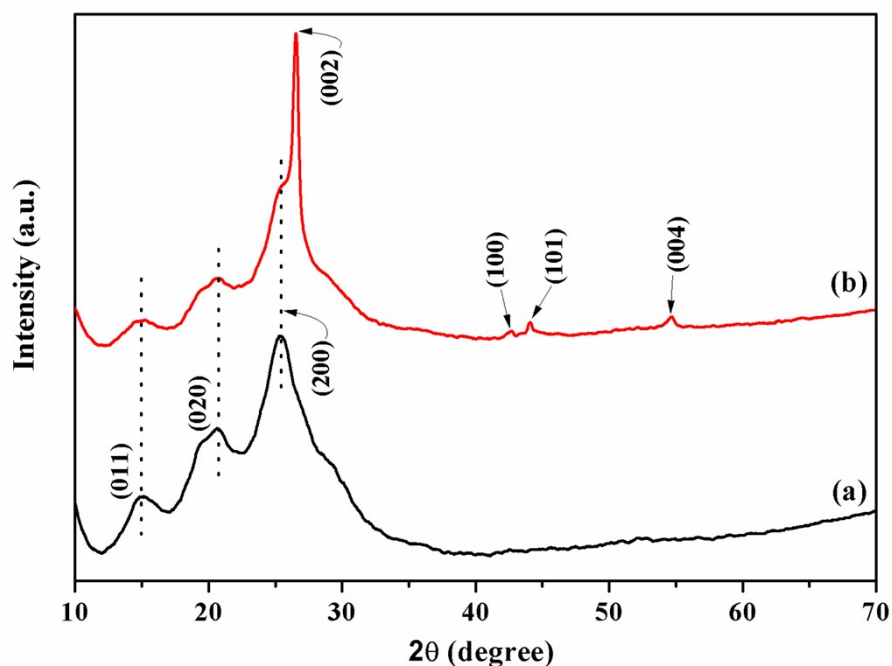


Fig. S2 XRD patterns of (a) pure PANI and (b) PG composite.

Raman Spectral Analysis

For the structural elucidation, the Raman spectroscopy was performed and the results are shown in Fig. S3. The major bands observed in the Raman spectrum of pure PANI (Fig. S3a) are at 525, 1161, 1219, 1335, 1469, 1591 cm^{-1} , which denote out of plane C–N–C torsion, C–H bending (in-plane) in the quinoid ring, C–N stretching, C–N⁺ stretching vibration (semiquinone radical structure), stretching of C=C in quinoid and in benzenoid ring, respectively.^{7,8} The peaks at $\sim 1338 \text{ cm}^{-1}$ (D-band) and $\sim 1594 \text{ cm}^{-1}$ (G-band) in the Raman spectrum of PG composite (Fig. S3b) confirm the presence of GNP in the composite.⁷

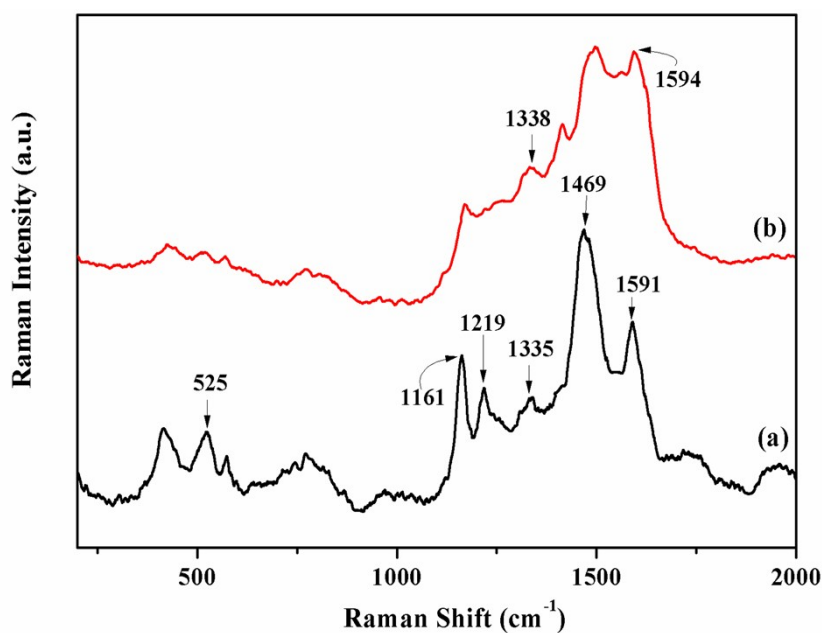


Fig. S3 Raman spectra of (a) PANI and (b) PG composite.

Morphological Analysis

FESEM has been carried out for the morphological studies of the PANI and PG composite and the obtained microstructures are shown in Fig. S4. The FESEM image of the pure PANI (Fig. S4a) reveals the appearance of fibre-like morphology indicating the formation of PANI through *in-situ* polymerization of aniline. Again, the FESEM image of the PG composite (Fig. S4b) indicates the random attachment of fibre-like PANI on the surface of well dispersed conducting GNPs as well as inside the graphene layers (indicated by light-green arrows in Fig. S4b) restricting the restacking of the individual graphene layers. This adherence and intercalation of fibre-shaped PANI into the GNP layers helps in the formation of a conducting network in the PG composite facilitating the intensive π - π interactions which finally lead to the elevated specific capacitance value, obtained for the PG composite.

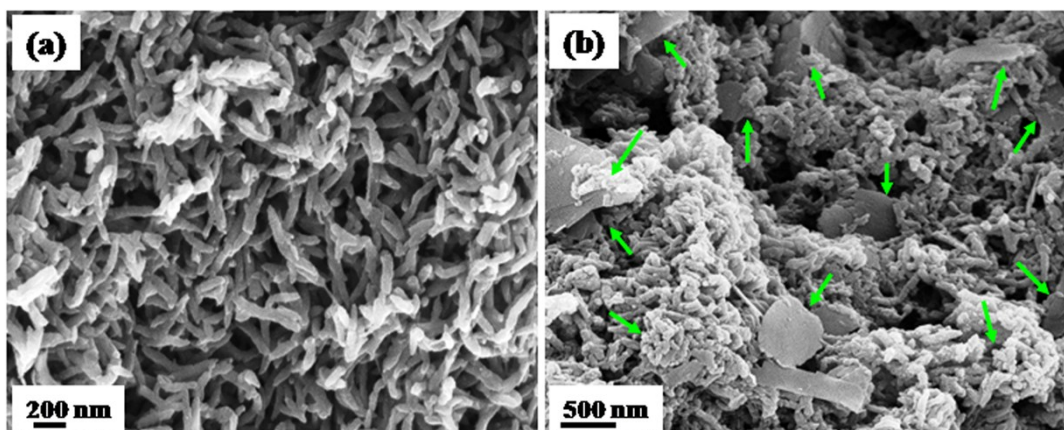


Fig. S4 FESEM micrographs of (a) pure PANI and (b) PG composite.

Electrochemical Characterizations of pure PANI, GNP and PG composite

The electrochemical performances of the electrode materials were explored by cyclic voltammetry (CV) and cyclic charge–discharge (CCD) measurements in the three electrode system in 1 M KNO_3 electrolyte. Fig. S5a illustrates the CV profiles of all the three electrodes with the same weight tested at a scan rate of 2 mV s^{-1} . The PG composite shows superior electrochemical characteristics than the other two electrode materials (pure PANI and GNP) within the working potential range of -0.5 to 0 V (vs. SCE) as it exhibits larger rectangular area. The enlarged CV area of the PG composite is the consequence of the double layer contribution of well-separated graphene plates along with the pseudocapacitive contribution of the conducting polymer, i.e., PANI. Again, Fig. S5b shows the CCD plots of all the three electrode materials together at the current density of 1 A g^{-1} . For any of the plots, no clear IR drop is noticed, which indicates the electrode materials have minute internal resistance. The obtained specific capacitance (C_s) values for pure PANI, GNP and PG composite are 135, 201 and 340 F g^{-1} , respectively (Table S1). Also, better rate capability of the PG composite is easily perceived from the Fig. S5f. In the PG composite, the presence of highly conducting GNP reduces the resistance, which, in turn, facilitates the electrochemical properties of the PG composite. Moreover, the introduction of thread-like PANI restricts the

restacking of the graphene platelets and hence this promotes the diffusion of the electrolyte ions into the composite electrode.

The C_{sp} values obtained for the electrode materials have been tabulated as below:

Table S1 C_{sp} values obtained for different electrode materials calculated from CCD measurements at different current densities

Current density (A g ⁻¹)	C_{sp} (F g ⁻¹) of different electrode materials		
	PANI	GNP	PG
1	135	201	340
2	83	177	317
3	66	164	300
5	48	153	280

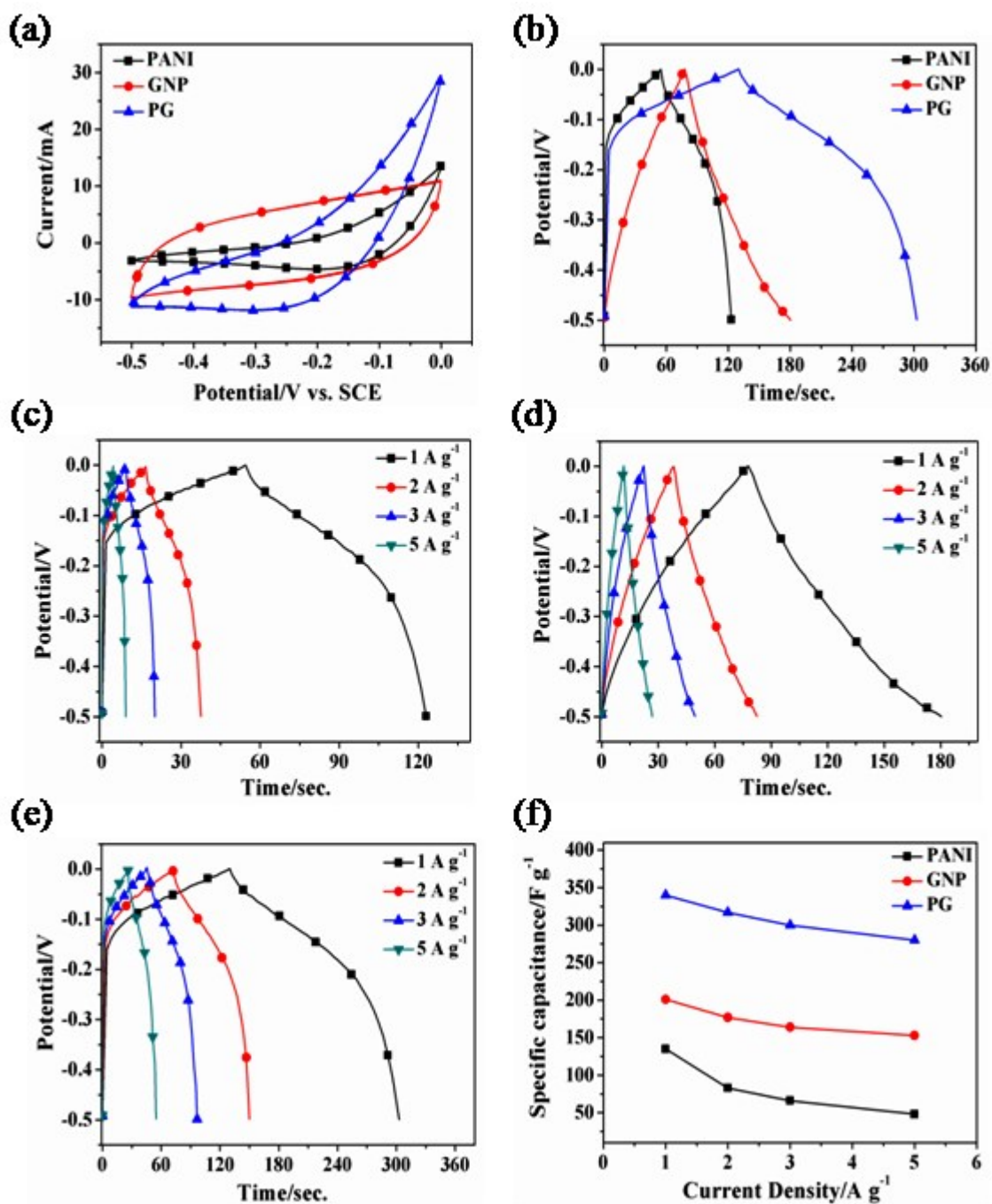


Fig. S5 Cyclic voltammograms of PANI, GNP and PG composite at 2 mV s^{-1} scan rate (a), CCD plots of PANI, GNP and PG composite at the current density of 1 A g^{-1} (b), CCD curves of PANI (c), GNP (d) and PG composite (e) at several current densities and variation of their calculated specific capacitances with those current densities (f).

Thermogravimetric Analysis

To verify the actual content (weight %) of the components in the hybrid, thermogravimetric analyses of the different materials were done by TGA-209F, Netzsch, Germany within the temperature range of 30–800 °C under air nitrogen atmosphere at the heating rate of 10 °C/min and the obtained results are recorded in Fig. S6. The thermogravimetric decomposition of PB has two sections and total weight loss at 800 °C is around 51.4%. The first stage of degradation from room temperature to around 370 °C corresponds to the removal of the water of crystallisation and the second stage of degradation might be due to decomposition of cyano group ultimately leading to the formation of iron oxide at 800 °C.⁹ On the other hand, the TGA plot of MnO₂ also shows two-step degradation process. At the first step from room temperature to around 230 °C, the degradation indicates the removal of absorbed water and the subsequent weight loss is attributed to the formation of Mn₂O₃ from MnO₂.¹⁰ Finally, the PB@MnO₂ hybrid shows the residual content of about 84.8% at 800 °C, which is very close to the residual mass (86.4%) of pure MnO₂ at the same temperature. Thus, it can be assumed that the residual mass of the hybrid at 800 °C under TGA experiment is mainly due to the presence of MnO₂ in the hybrid. Therefore, the amount of MnO₂ in the hybrid could be calculated as ~ 36.2%.¹¹

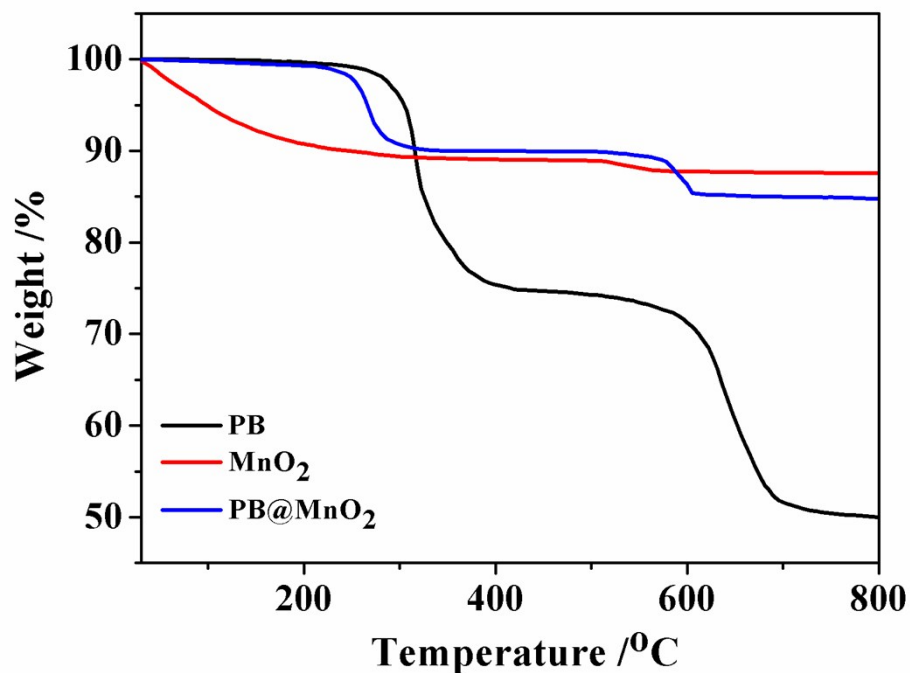


Fig. S6 TGA curves of PB, MnO₂ and PB@MnO₂ hybrid.

Measurement of average thickness and the estimated thickness of the MnO₂ deposited on PB microcubes in the PB@MnO₂ hybrid

The average thickness of the MnO₂ grown on PB microcubes in the PB@MnO₂ hybrid was measured from various regions of the several TEM micrographs of the PB@MnO₂ hybrid. The average thickness is found to be ~ 62 nm.

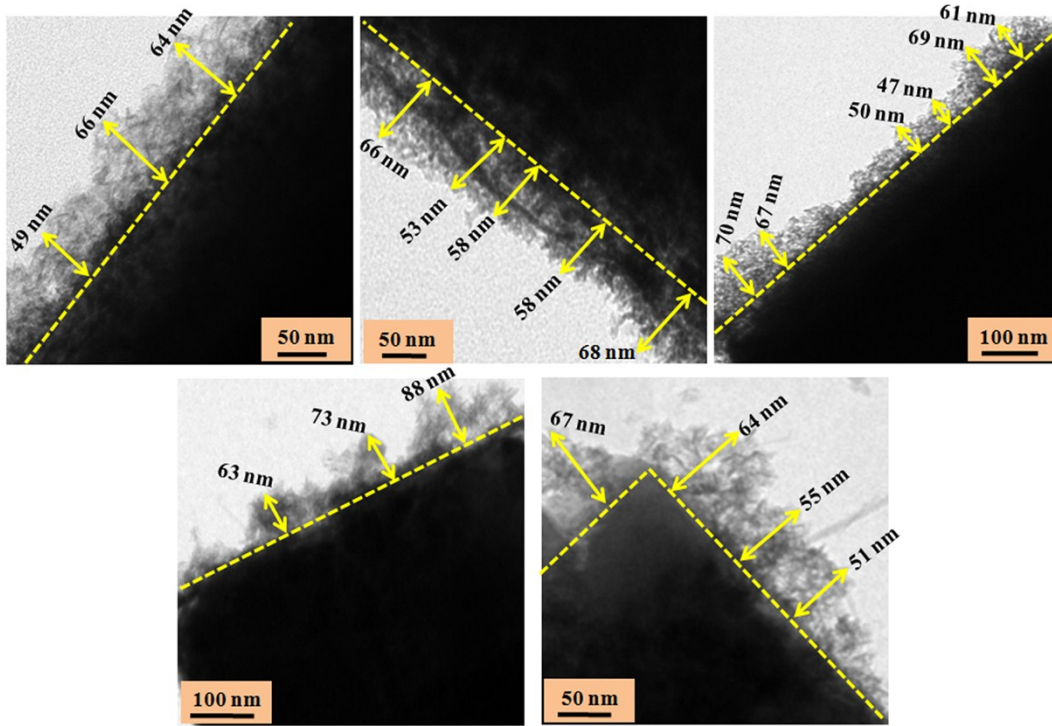


Fig. S7 Measurement of average thickness of MnO₂ grown of PB microcubes from various regions of the TEM micrographs of the PB@MnO₂ hybrid.

The layer thickness (h) of the deposited MnO₂ on the external surface area (S_{ext}) of the PB microcubes can also be estimated based on the mass ratio of MnO₂ to PB and using the bulk density of MnO₂ (ρ_{MnO_2}) = 5.026 g cm⁻³ following the equation:¹²

$$h = \frac{m_{MnO_2}}{m_{PB}} \cdot \rho_{MnO_2}^{-1} \cdot S_{ext}^{-1} \quad (S1)$$

While estimating the layer thickness (h), it is assumed that all mass of MnO₂ is deposited on the external surface area of the PB microcubes. Based on all the data, the thickness of MnO₂ is estimated as ~ 14 nm.

Here, it is interesting to observe that the actual average thickness measured from TEM micrographs of PB@MnO₂ hybrid differs much from the estimated thickness based on the mass ratio of MnO₂ and surface area of PB. This difference between actual thickness and estimated thickness is probably due to the limitation in the thickness measurement (along Z-

axis) from TEM micrographs as the obtained TEM micrographs are absolutely two dimensional images. Now, in order to obtain the thickness from the TEM micrographs, it is necessary to measure the layer thickness of the deposited MnO₂ along Z-axis on the side of PB microcubes, which is impossible to do from the TEM micrographs.

Electrochemical Characterizations of pure MnO₂

The electrochemical feature of pure mesoporous MnO₂ was also investigated in a three-electrode electrochemical cell with a Pt counter electrode and the saturated calomel electrode (SCE) as the reference one in 1 M KNO₃ aqueous solution as the electrolyte and Fig. S8 shows the obtained results. Fig S8a represents the cyclic voltammograms (CVs) of MnO₂ at different scan rates (e.g., 2, 5, 10, 30 and 50 mV s⁻¹) in the potential window of -0.2 to +0.6 V. The quasi-rectangular shaped CV profiles of the MnO₂ denotes its pseudocapacitive nature and this might be due to the intercalation-deintercalation of the K⁺ ions along with the interconversion between Mn^{III} and Mn^{IV}, as reported elsewhere.¹³ At higher scan rates, the electrolytic cations cannot access the bulk electrode material fully and hence, limited intercalation-deintercalation process leads to decrease in pseudocapacitive activities of MnO₂.^{13,14} The cyclic charging and discharging (CCD) measurements were done at several current densities (e.g., 1, 2, 3 and 5 A g⁻¹) within the same voltage window and the obtained CCD plots almost look like a equilateral triangle, as illustrated in Fig. S8b. This shape of the CCD plots is indicative of the fast and highly reversible faradic process occurring in the oxide electrode material during CCD measurement.¹³ It is also observed from Fig. S8b that the CCD plot shows longer discharging time at lower current density and this is owing to the sufficient adsorption and intercalation of the K⁺ ions during CCD process when current density is low. Now, the calculation of the specific capacitance value (C_{sp}) of the electrode material was made from discharging curve using the equation as follows:

$$C_{sp} = \frac{I \times \Delta t}{m \times \Delta V}$$

Where, I (A), Δt (s), m (g) and ΔV (V) represent the discharging current, discharging time, mass of the active material in the electrode and the potential in this CCD process, respectively. The calculated C_{sp} of MnO₂ was 160 F g⁻¹ at the current density of 1 A g⁻¹. Moreover, at the higher current density of 5 A g⁻¹, the MnO₂ retains around 58% of its capacitance (93 F g⁻¹). These results are attributed to the mesoporous structure of MnO₂, which shortens the ion diffusion path ensuring the high utilization of the active material. Finally, Fig. S8c represents the variation of obtained C_{sp} with the current densities showing the decrease in C_{sp} with increase in the current densities.

The C_{sp} values obtained for the MnO₂ have been tabulated as below:

Table S2 C_{sp} values obtained for MnO₂ calculated from CCD measurements at different current densities

Current Density (A g ⁻¹)	C_{sp} (F g ⁻¹)
1	160
2	134
3	112
5	93

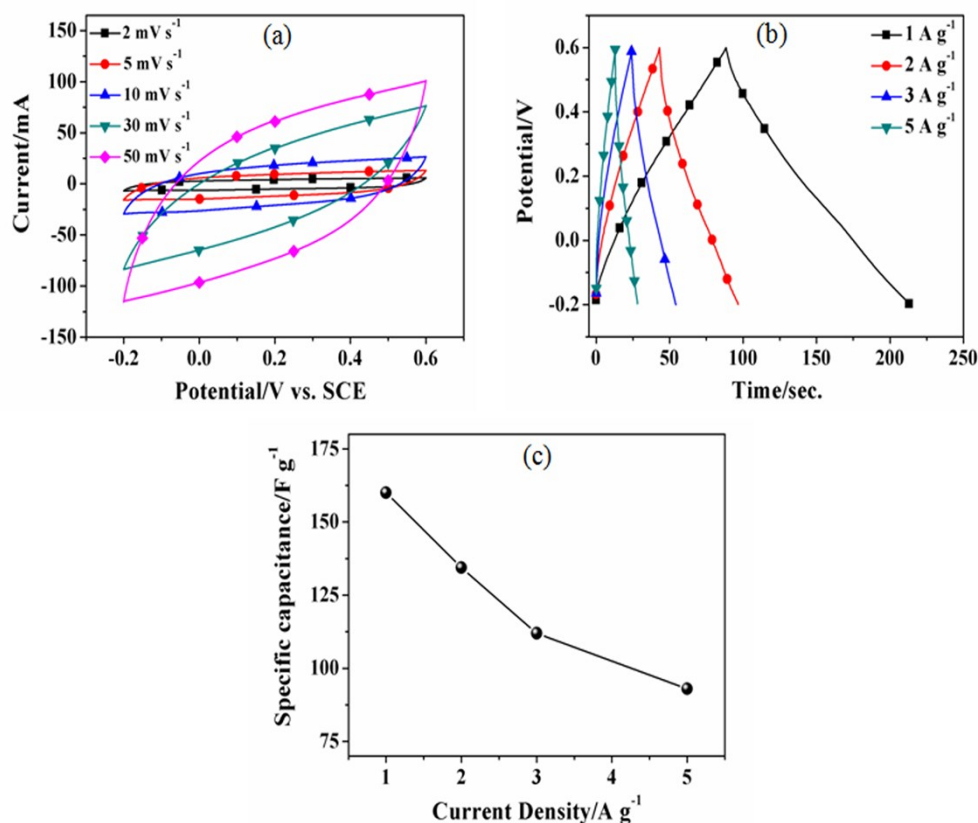


Fig. S8 Cyclic voltammograms of pure MnO₂ at different scan rates (a), CCD plots of pure MnO₂ at several current densities (b), variation of their calculated specific capacitances with those current densities (c).

Workability test of PB@MnO₂//PG ASC device within different potential windows:

In this work, the working potential windows of PG (the negative electrode material) and PB@MnO₂ hybrid (positive electrode material) are -0.5 to 0.0 V and -0.2 to 0.6 V (vs. SCE), respectively, which indicate that the operating voltage window of the PB@MnO₂//PG ASC can be 1.1 V and the CV profile of the device obtained at the scan rate of 5 mV s⁻¹ within the potential window of 1.1 V is shown by Fig. S9a. But, this is not the ultimate potential range of the PB@MnO₂//PG ASC. To support this, the CV measurement of the ASC device within different operating cell voltage ranges (varying from 0–0.8 V to 0–1.9 V) at 5 mV s⁻¹ scan rate was also performed and Fig. S9b represents the obtained cyclic

voltammograms of the ASC device. Now, it can be observed from the figures that the ASC retains the shape of the CV profile even at a maximum cell voltage of 1.9 V, which suggests long-term stable electrochemical performance under wide operating potential windows of the ASC device. These experimental results indicate that the ultimate potential of the ASC is not limited to 1.1 V, rather it can work within a high potential window of 1.9 V.

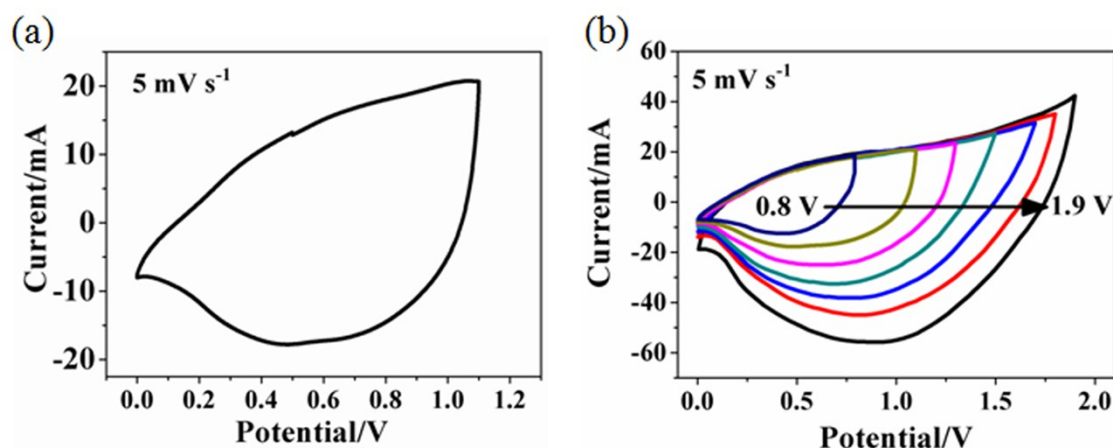


Fig. S9 (a) Cyclic voltammogram of the assembled PB@MnO₂//PG ASC device collected within the potential window of 1.1 V at 5 mV s⁻¹ scan rate and (b) CV curves of the same ASC device at different scan potential windows at 5 mV s⁻¹ scan rate.

Reference:

- 1 A K. Das, S. K. Karan and B. B. Khatua, *Electrochim. Acta*, 2015, **180**, 1–15.
- 2 B. Abad, I. Alda, P. Díaz-Chao, H. Kawakami, A. Almarza, D. Amantia, D. Gutierrez, L. Aubouy and M. Martín-González, *J. Mater. Chem. A*, 2013, **1**, 10450–10457.
- 3 X. M. Feng, R. M. Li, Y. W. Ma, R. F. Chen, N. E. Shi, Q. L. Fan, and W. Huang, *Adv. Funct. Mater.*, 2011, **21**, 2989–2996.
- 4 G. D. Vuković, A. D. Marinković, M. Čolić, M. Đ Ristić, R. Aleksić, A. A. Perić-Grujić and P. S. Uskoković, *Chem. Eng. J.*, 2010, **157**, 238–248.
- 5 N. A. Kumar, H. J. Choi, Y. R. Shin, D. W. Chang, L. Dai and J. B. Baek, *ACS nano*, 2012, **6**, 1715–1723.

- 6 R. Rajarao and B. R. Bhat, *Nanomater. Nanotechnol.*, 2012, **2**, 1–6.
- 7 X. Xia, Q. Hao, W. Lei, W. Wang, H. Wang and X. Wang, *J. Mater. Chem.*, 2012, **22**, 8314–8320.
- 8 D. Xu, Q. Xu, K. Wang, J. Chen and Z. Chen, *ACS Appl. Mater. Interface*, 2013, **6**, 200–209.
- 9 Z. Jiang, D. Jiang, A. S. Hossain, K. Qian and J. Xie, *Phys. Chem. Chem. Phys.*, 2015, **17**, 2550-2559.
- 10 T. Liu, G. Shao, M. Ji and G. Wang, *J Solid State Chem.*, 2014, **215**, 160-166.
- 11 C. Mao, S. Liu, L. Pang, Q. Sun, Y. Liu, M. Xu and Z. Lu, *RSC Adv.*, 2016, **6**, 5184-5191.
- 12 C. Weber, V. Lormann, G. Reichenauer and J. Pflaum, *arXiv preprint arXiv:1411.6278*, 2014.
- 13 Y. Wang and Q. Chen, *ACS Appl. Mater. Interfaces*, 2014, **6**, 6196–6201.
- 14 W. Chen, R. B. Rakhi and H. N. Alshareef, *J. Mater. Chem.*, 2012, **22**, 14394.